JOURNAL OF GEOPHYSICAL RESEARCH, VOL. 115, A07305, doi:10.1029/2009JA014956, 2010

Climatological patterns of high-latitude convection in the Northern and Southern hemispheres: Dipole tilt dependencies and interhemispheric comparisons

E. D. Pettigrew,[1] S. G. Shepherd,[1] and J. M. Ruohoniemi[2]

Received 2 October 2009; revised 25 February 2010; accepted 8 March 2010; published 13 July 2010.

[1] Using line-of-sight measurements of horizontal plasma drift from the Super Dual Auroral Radar Network (SuperDARN) located in the Northern and Southern hemispheres over a period extending from 1998 to 2002, statistical models of the high-latitude convection electric field are derived for various ranges of interplanetary magnetic field (IMF) magnitude and orientation and for several ranges of dipole tilt angle. Direct comparison of the corresponding convection patterns in each hemisphere shows that under neutral tilt conditions (dipole tilt angle magnitude <10°) the patterns are most similar. However, a strong dipole tilt angle dependence is observed under northward (B_z+) and B_y dominated IMF conditions. For IMF B_z+, reverse convection is observed to be much stronger during positive tilt than negative tilt. For IMF B_y dominated conditions (IMF B_z = 0), the round convection cell is more enhanced for positive tilt than for negative tilt, particularly for IMF B_y < 0 in both hemispheres. The presence of a lobe cell is a likely cause of this enhancement, although it is not entirely clear why it occurs preferentially under IMF B_y < 0. In addition, the crescent-shaped cells are weakened as tilt angle progresses from negative to positive, most likely due to vastly different solar produced conductivities under different tilt angles. For IMF B_z−, asymmetric values of the cross-polar cap potentials (Φ_{PC}) are observed between hemispheres, with Φ_{PC} in the south being systematically larger than Φ_{PC} in the north. Although neutral tilt patterns are similar enough to be used interchangeably, convection has a strong dipole tilt dependence and a Northern Hemisphere convection model should not be applied to the Southern Hemisphere if dipole tilt angle is not taken into account. When dipole tilt is accounted for, Φ_{PC} differs between hemispheres by less than 10% on average, but the strength of the convection in the individual cells differs by 15% to 20% on average.

Citation: Pettigrew, E. D., S. G. Shepherd, and J. M. Ruohoniemi (2010), Climatological patterns of high-latitude convection in the Northern and Southern hemispheres: Dipole tilt dependencies and interhemispheric comparisons, *J. Geophys. Res.*, *115*, A07305, doi:10.1029/2009JA014956.

1. Introduction

[2] In the Earth's polar ionosphere the convection electric field is primarily due to the communication of unattenuated magnetospheric convection electric fields, driven by magnetic reconnection at the dayside magnetopause and in the Earth's magnetotail, to ionospheric altitudes. To some extent, field-aligned potential structures, ionospheric conductivity structure, and neutral winds also act to modulate the observed electric field. Theoretical and observational studies have documented many details of ionospheric convection on a variety of spatial and temporal scales, including how it responds to changes in the solar wind and interplanetary magnetic field (IMF) [e.g., *Cowley*, 1982; *Wygant et al.*, 1983; *Siscoe and Huang*, 1985; *Fedder and Lyon*, 1987; *Cowley and Lockwood*, 1992; *Ruohoniemi et al.*, 2002; *Lester et al.*, 2006; *Chisham et al.*, 2007].

[3] The global-scale pattern of convection represents, to a large extent, a measure of the coupling between the solar wind and the magnetosphere-ionosphere (M-I) system and is useful in studies of this coupled system [e.g., *Heppner*, 1972; *Reiff et al.*, 1981; *Fedder et al.*, 1991; *Ridley*, 2005]. However, because measurements of the global instantaneous convection electric field are not yet possible, statistical or climatological patterns are often used as a proxy for or to augment available measurements. In addition, the convection electric field is an important source of energy to the upper atmosphere and must be specified completely in many models of this region [e.g., *Fuller-Rowell et al.*, 1996; *Ridley et al.*, 2006; *Schunk et al.*, 2004]. For these

[1]Thayer School of Engineering, Dartmouth College, Hanover, New Hampshire, USA.
[2]Bradley Department of Electrical and Computer Engineering, Virginia Polytechnic Institute and State University, Blacksburg, Virginia, USA.

0148-0227/10/2009JA014956

reasons and others, numerous statistical or climatological convection electric field maps have been developed based on a variety of data sets including those from polar orbiting spacecraft such as OGO 6 [*Heppner*, 1977; *Heppner and Maynard*, 1987], AE and DE 2 [*Lu et al.*, 1989], DE 2 [*Weimer*, 1995, 1996, 2001, 2005], and Defense Meteorological Satellite Program (DMSP) [*Rich and Hairston*, 1994; *Boyle et al.*, 1997; *Papitashvili and Rich*, 2002], linear regression relationships between solar wind parameters, ground-based magnetometers, and DMSP data such as the Institute of Terrestrial Magnetism, Ionosphere and Radiowave Propagation (IZMIRAN) Electrodynamic Model (IZMEM) [*Papitashvili et al.*, 1994, 1999]; ionospheric line-of-sight (LOS) convection velocities from ground-based incoherent backscatter radars [*Foster et al.*, 1986; *Holt et al.*, 1987; *Zhang et al.*, 2007] and coherent backscatter radars [*Ruohoniemi and Greenwald*, 1996, 2005].

[4] Climatological models represent the average convection electric field that is observed when some independently-measured condition or parameter falls within a specified range. The conditions used to parameterize a climatological model typically include the transverse magnitude of the IMF, $B_T = \sqrt{B_y^2 + B_z^2}$, and clock angle, $\theta = atan(B_z/B_T)$. B_y and B_z are the y- and z-components of the IMF in geocentric solar magnetospheric (GSM) coordinates, respectively. In some cases the solar wind velocity or dynamic pressure or indices of geomagnetic activity such as K_p are used as well as or instead of these.

[5] Most studies that result in climatological patterns do not distinguish between observations made in the Northern and Southern hemispheres. Some studies are limited to Northern Hemisphere data [e.g., *Zhang et al.*, 2007; *Ruohoniemi and Greenwald*, 1996, 2005] while others combine Southern Hemisphere data with Northern Hemisphere data to increase the amount of data [*Weimer*, 2005; *Boyle et al.*, 1997]. In these cases, it is assumed that convection in the two hemispheres is symmetric under opposite signs of IMF B_y. This simplifying assumption should hold to the extent that both hemispheres have symmetric magnetic fields and conductivities [e.g., *Tanaka et al.*, 2001; *Watanabe et al.*, 2007].

[6] Making this assumption, it is therefore possible to use a Northern Hemisphere convection model when a model of the Southern Hemisphere is needed. In the technique described by *Ruohoniemi and Baker* [1998] and *Shepherd and Ruohoniemi* [2000], global-scale convection patterns are obtained by fitting LOS velocity measurements from the Super Dual Auroral Radar Network (SuperDARN) to a functional form of the electrostatic potential. In this procedure, the instantaneous LOS vectors are supplemented with model data sampled from the appropriate statistical pattern of *Ruohoniemi and Greenwald* [1996] (referred to hereafter as RG96) in regions where instantaneous data are unavailable, preventing the solution from becoming unphysical [*Shepherd and Ruohoniemi*, 2000]. This technique has been applied to SuperDARN data in the Southern Hemisphere by flipping the sign of the IMF B_y component in the RG96 convection model and applying that Northern Hemisphere model to the Southern Hemisphere [e.g., *Lukianova et al.*, 2008].

[7] A question remains as to what extent it is valid to assume that Northern and Southern hemisphere observations can be used interchangeably after simply switching the sign of IMF B_y. Owing to observed differences between the geomagnetic field in the Northern and Southern hemispheres, such as the ~8° difference in the locations of the geomagnetic poles relative to the corresponding geographic poles [*Mandea and Macmillan*, 2000] and the presence of the South Atlantic Anomaly [e.g., *Zmuda*, 1966], it would seem more correct to use a convection model derived from measurements taken in the appropriate hemisphere.

[8] Case studies by *Knipp et al.* [1993, 2000] and *Lu et al.* [1994] used ground-based magnetometer measurements combined with satellite and sometimes ground-based radar measurements using the Assimilative Mapping of Ionospheric Electrodynamics (AMIE) technique [*Richmond and Kamide*, 1988] to derive patterns for both hemispheres, showing significant interhemispheric asymmetries in the strengths and configurations of the convection.

[9] In this study we use data from the SuperDARN radars and apply the analytical approach of *Ruohoniemi and Greenwald* [2005] (hereafter referred to as RG05) to derive statistical patterns for both the Northern and Southern hemispheres with the overall aims of an improved understanding of dipole tilt factors in the northern patterns and of making direct comparisons of statistical patterns derived in a consistent manner for the two hemispheres. Thus, while adjustment factors on the SuperDARN velocity measurements are now under discussion [e.g., *Gillies et al.*, 2009], we have performed the analysis with the velocities derived in the conventional manner. Considerations of the impacts of velocity adjustments, solar cycle, etc., are discussed briefly but largely deferred to later work. In addition, while variability in the ionospheric plasma velocities is pronounced [e.g., *Codrescu et al.*, 1995, 2000; *Crowley and Hackert*, 2001; *Matsuo et al.*, 2003; *Shepherd et al.*, 2003], in this paper (as in its predecessors) we focus on the quasi-stationary patterns expected for periods of prolonged, quasi-static solar wind conditions. The analysis has rendered much information on the variability in the velocity measurements which is also discussed briefly but will be examined in future work.

[10] The resulting patterns for the Northern Hemisphere are similar to those obtained by RG05 although slight differences in data processing were necessary and are described in section 2. In section 3 the similarities and differences observed between the patterns in each hemisphere are described and a discussion of the observed differences and their possible causes follows in section 4.

2. Technique

[11] In order to make as direct a comparison of the two hemispheres as possible, the same data set and procedure were used to produce statistical convection patterns for both the Northern and Southern hemispheres. To maintain consistency with RG05 and with earlier studies to which it relates, we have adopted the same criteria on data selection, data type, binning, and processing; the one deviation is the consideration of dipole tilt in place of a pure seasonal factor. This procedure is described in RG05 but a summary is included here. Furthermore, we have analyzed the same time period, January 1998–December 2002. Figure 1 shows the fields of view of the nine radars in the Northern Hemisphere and the six radars in the Southern Hemisphere that were operational during this time period.

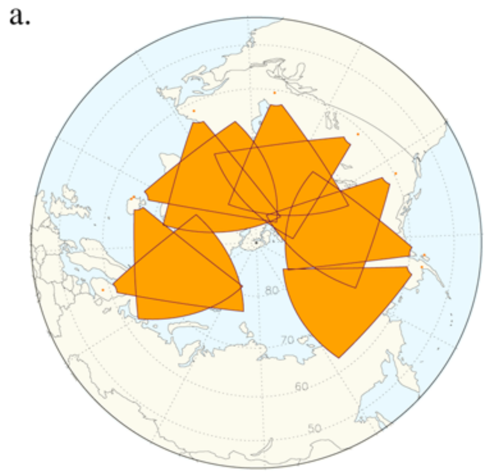

Figure 1. Fields of view of (a) Northern Hemisphere and (b) Southern Hemisphere radars.

[12] The first step in deriving statistical patterns involves sorting data into categories based on some predetermined conditions. As with RG05, we classify the data into twenty-four categories based on the prevailing IMF condition, using three B_T magnitude bins 0–3 nT, 3–5 nT, and 5–10 nT and eight 45°-wide clock angle bins centered about 0° (B_z+), 45° (B_z+/B_y+), etc. In addition, several studies have identified a seasonal dependence in the convection pattern [e.g., RG05; *Rich and Hairston*, 1994; *Weimer*, 2005]. For this reason we choose to further separate the data according to 'seasonal' bins based on the dipole tilt angle. Note that, due to the offset between the Earth's dipole axis and rotation axis, the tilt angle can vary by about 20° in any given day and there is not actually a one-to-one correlation between dipole tilt and season. Furthermore, in this paper the sign of the dipole tilt angle is switched in the Southern Hemisphere to allow direct comparison with the Northern Hemisphere. We use this sign-adjusted dipole tilt angle, hereafter referred to simply as tilt, to sort our data since it is a more accurate measure of the Earth's magnetic field geometry and of the amount of solar-produced ionospheric conductivity (possible sources of the observed dependence). The tilt is calculated using the International Geomagnetic Reference Field (IGRF) model [*Mandea and Macmillan*, 2000] and the data are classified as: negative tilt (tilt < −10°), neutral tilt (−10° < tilt <10°), or positive tilt (tilt >10°). Time periods during which the tilt is negative come primarily from winter months, and positive come primarily from summer months. These relations are utilized to compare the results of this study to previous studies which sort by true season.

[13] The time period used in this study (1998–2002) spans almost half of Solar Cycle 23, centered slightly before the cycle maximum. IMF data for this time period are obtained by lagging observations from the Advanced Compositions Explorer (ACE) spacecraft, given in GSM coordinates, to the subsolar magnetopause. As with RG05, the lag time is determined using a simple ballistic calculation based on the local solar wind velocity. In order to account somewhat for uncertainties in this estimate of the lag, non-overlapping 12-minute means of the three IMF components are used and only those periods during which the same IMF condition persists for at least 36 minutes are used in the study. Figure 2 shows how all of the 12-minute intervals in the study period are distributed in the 24 IMF bins selected. The distribution of IMF magnitudes maximizes in the 3–5 nT bin, but there is excellent coverage across the entire magnitude range 0–10 nT. The distribution of IMF clock angles maximizes near IMF B_z = 0.

[14] The LOS velocity data from all operational radars in each hemisphere from all the 12-min time periods are collected and sorted by IMF condition and tilt as described above. For a given IMF and tilt condition, all of the corresponding LOS velocity vectors are mapped to an equal-area grid in magnetic latitude and magnetic local time (MLT), where each cell spans 1° magnetic latitude. Each equal-area grid cell can contain from three to several thousand vectors. An example of the spatial distribution of LOS mea-

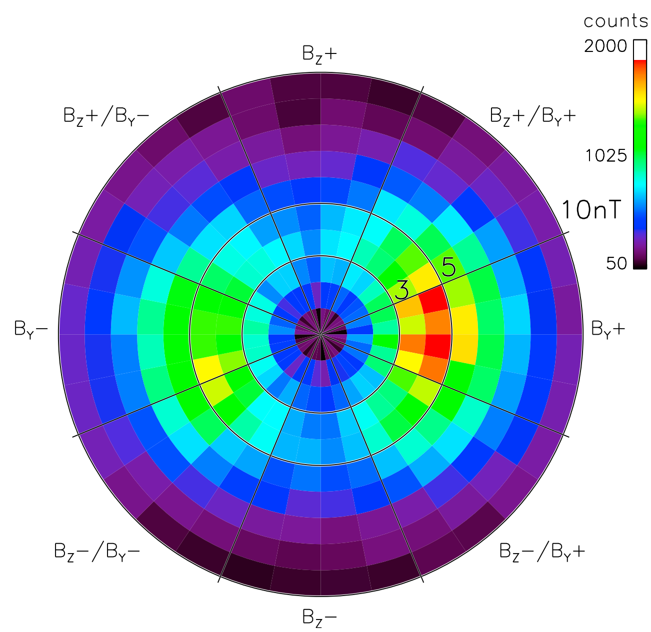

Figure 2. Statistical distribution of the IMF clock angle and transverse magnitude at the magnetopause, lagged from ACE.

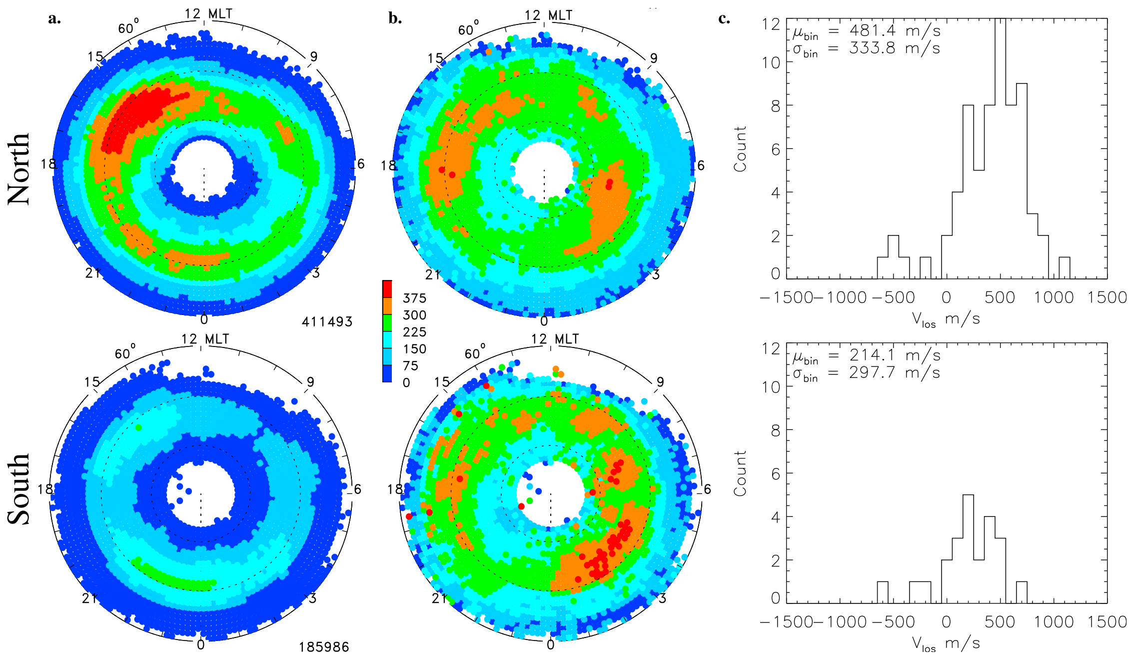

Figure 3. Distribution of (a) LOS measurements and (b) variability in 1° equal-area grid cells for 5–10 nT, B_z- for the (top) Northern and (bottom) Southern hemispheres for neutral tilt (−10° < tilt <10°). The same color scale at center indicates number (Figure 3a) and standard deviation in m/s (Figure 3b) of the LOS measurements in the cell. Total number of data points is giving at bottom right in Figure 3a. (c) Distribution of LOS magnitudes in a random cell in the cusp region (near 75° latitude, 12 MLT, poleward look direction) for the same IMF and tilt conditions. Values of the mean and standard deviation are shown at top left.

surements in both hemispheres is shown in Figure 3a for IMF B_T = 5–10 nT, IMF B_z-, neutral tilt.

[15] Because there are fewer radars in the Southern Hemisphere (5–6 in the south as opposed to 8–9 in the north), there are, in general, fewer LOS velocity measurements available in the Southern Hemisphere than in the Northern Hemisphere. Due to propagation condition effects and plasma instability conditions there is in general more backscatter during the winter than the summer [*Ruohoniemi and Greenwald*, 1997; *Koustov et al.*, 2004].

[16] In general, the backscatter occurrence rate maximizes near auroral latitudes (usually peaking around 70°). It falls off near the poles as distance from the radar locations exceeds 3,000 km and falls off for latitudes below 60° (equatorwards of the radar locations). Due to the compressed shape of the dayside magnetosphere, the occurrence rates fall off with decreasing latitude more quickly on the dayside than on the nightside. The occurrence rates also vary with MLT, typically maximizing on the nightside, although this MLT dependence changes with IMF condition.

[17] As in RG05, all the LOS vectors in a given grid cell are sorted by their azimuthal direction into bins which span 10° and are centered at 0°, 10°, 20°, etc. All the vectors within a given azimuth angle bin are averaged together, such that a maximum of 36 vectors per grid cell are stored, reducing the data set. As an estimate of variability in the velocities, the standard deviations of the vectors in each 10° azimuth bin are also calculated and used as error-weights in the fitting procedure.

[18] Figure 3c shows the distribution of LOS magnitudes in one 10° azimuth bin from a random cell in the cusp region (near 75° latitude, 12 MLT, poleward look direction) for both hemispheres, for IMF B_T = 5–10 nT, IMF B_z-, neutral tilt. Although the sample sizes are small, making a rigorous test for normality difficult, the distributions do not appear significantly non-normal. Using the interquartile range as measure of variance and the median as a measure of the expected value in a subset of bins gave results consistent with the calculated means and standard deviations. While the underlying distribution may or may not be truly normal, the mean and standard deviation give meaningful estimates of the expected value and variance of the velocities in a given bin.

[19] An example map of the distribution of average velocity variability in both hemispheres in shown in Figure 3b, also for IMF B_T = 5–10 nT, IMF B_z-, neutral tilt. The median values are around 200 m/s and the maximum values are around 400 m/s. These variabilities are of the same order of magnitude as the LOS velocity magnitudes, which typically have a median value around 300 m/s and a maximum around 800 m/s. The standard deviation values maximize near auroral latitudes, corresponding with the maximum occurrence rates. They peak on the dayside in the pre- and post-noon sectors, where the number of measurements is large and the velocities values are high, and on the nightside in the post-midnight sector, near the low velocity convection reversal region. The distributions shown for this IMF and tilt condition are representative of the variability dis-

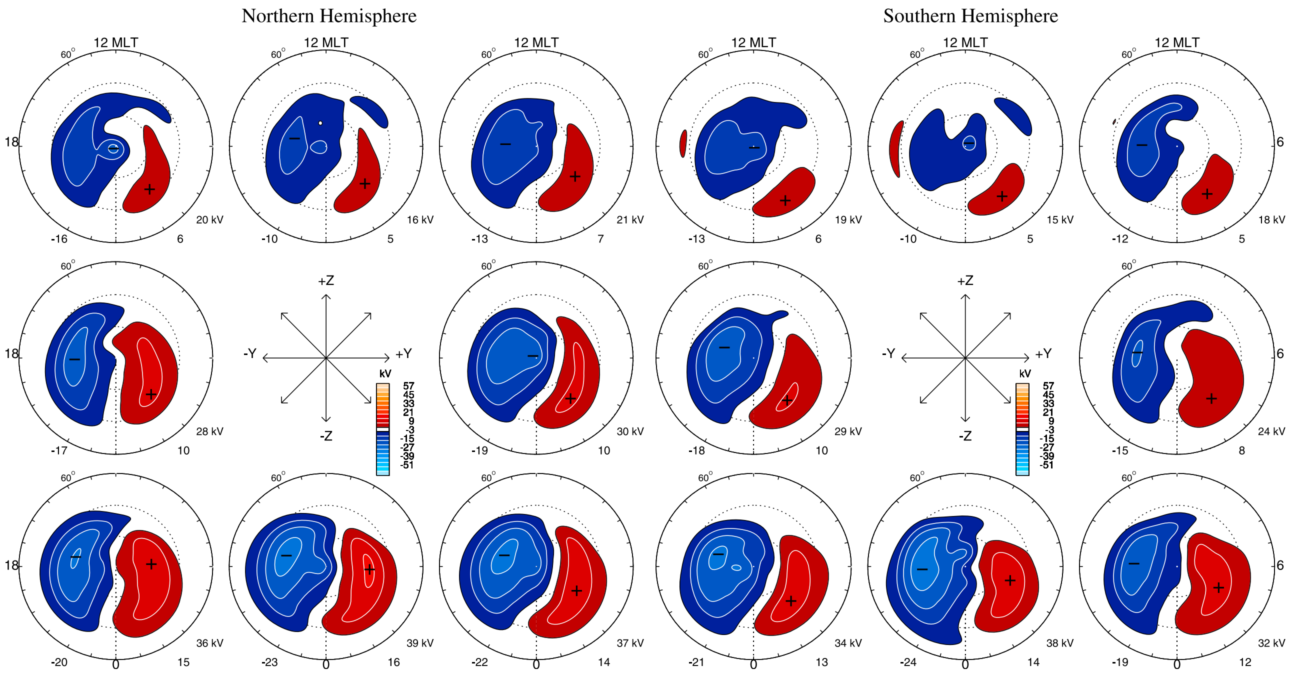

Figure 4. Statistical convection patterns sorted by IMF clock angle for 0 nT < B_T < 3 nT, neutral tilt. Color indicates the electric potential, with red (blue) shades corresponding to positive (negative) potentials as shown in the color bar at center. Equipotential contours are plotted at 6 kV intervals. For both hemispheres, the patterns are rotated so that noon (12 MLT) is at the top with dawn (06 MLT) on the right and dusk (18 MLT) on the left. All plots have a low-latitude boundary of 60°. Small numbers at bottom left and right indicate the potential minimum and maximum. Φ_{PC} is given in the bottom right.

tributions that are typically seen. Slightly higher standard deviation values are seen under negative tilt, when there are more data points, and slightly lower values are seen under positive tilt.

[20] Larger variability in a given cell indicates greater scatter in the velocities measured within that cell. Consequently, the ability of the resolved statistical pattern to predict a radar LOS velocity measurement in such a cell will be somewhat lower than it is over an area of lower variability. The presence of such variations in the observed velocities could be due to geophysical processes such as small-scale variability [e.g., *Codrescu et al.*, 1995] or motion of the large-scale pattern resulting from dayside [e.g., *Shepherd and Shubitidze*, 2003] or nightside magnetospheric reconnection [e.g., *Bristow and Jensen*, 2007]. It is also possible that some variability is due to enhanced absorption, particularly on the nightside during more active periods, as was noted by RG96. A more detailed study is needed to investigate the sources of the observed variability. In terms of the derivation of the statistical pattern, the data points with higher variabilities make a lessor contribution to the global result.

[21] It should also be noted that recent evidence suggests that the SuperDARN velocities usually underestimate the $\mathbf{E} \times \mathbf{B}$ velocity due to the unaccounted effect of refraction on HF group velocity near the reflection point [e.g., *Gillies et al.*, 2009]. The amount of underestimation and the degree to which it affects the climatological patterns remain to be worked out. For a limited set of observations, *Gillies et al.* [2009] found that the velocities obtained by the standard procedure are between 80–100% (typically 90%) of the values obtained by incorporating refractive effects. It is possible that some of the observed variability in the LOS velocities is due to variation in the index of refraction in the scattering region. We reiterate that we have used velocities derived using the standard procedure in order to obtain statistical patterns that are consistent with preexisting patterns, facilitating comparison with previous work and allowing for direct comparisons of the large-scale convection patterns in the two hemispheres. A complete resolution of the impact of this factor on the velocity determinations and potential patterns awaits implementation of more complete diagnostic measurements at the radars and is beyond the scope of this paper.

[22] The average velocity vectors, error-weighted using their corresponding standard deviation values, are fit to an 8th order, 8th degree expansion of spherical harmonics according to the method of *Ruohoniemi and Greenwald* [1998]. This expansion has a resolution of approximately 4° magnetic latitude and 1.5 hours MLT. The electrostatic potential distribution across the magnetic latitude, MLT grid $\Phi(\lambda, MLT)$ is calculated from the fitted velocities using the relationships $\mathbf{V} = (\mathbf{E} \times \mathbf{B})/B^2$, $\mathbf{E} = -\nabla\Phi$. Contour maps of the potential distribution are the most commonly used format for displaying the resulting convection patterns.

[23] As discussed in RG05 and *Shepherd and Ruohoniemi* [2000], we add an additional constraint to the fitted convection patterns by padding the low-latitude dayside with zero-velocity vectors. This influences the solution to match the compressed-dayside shape that the convection is expected to take [e.g., *Heppner and Maynard*, 1987]. In a sensitivity

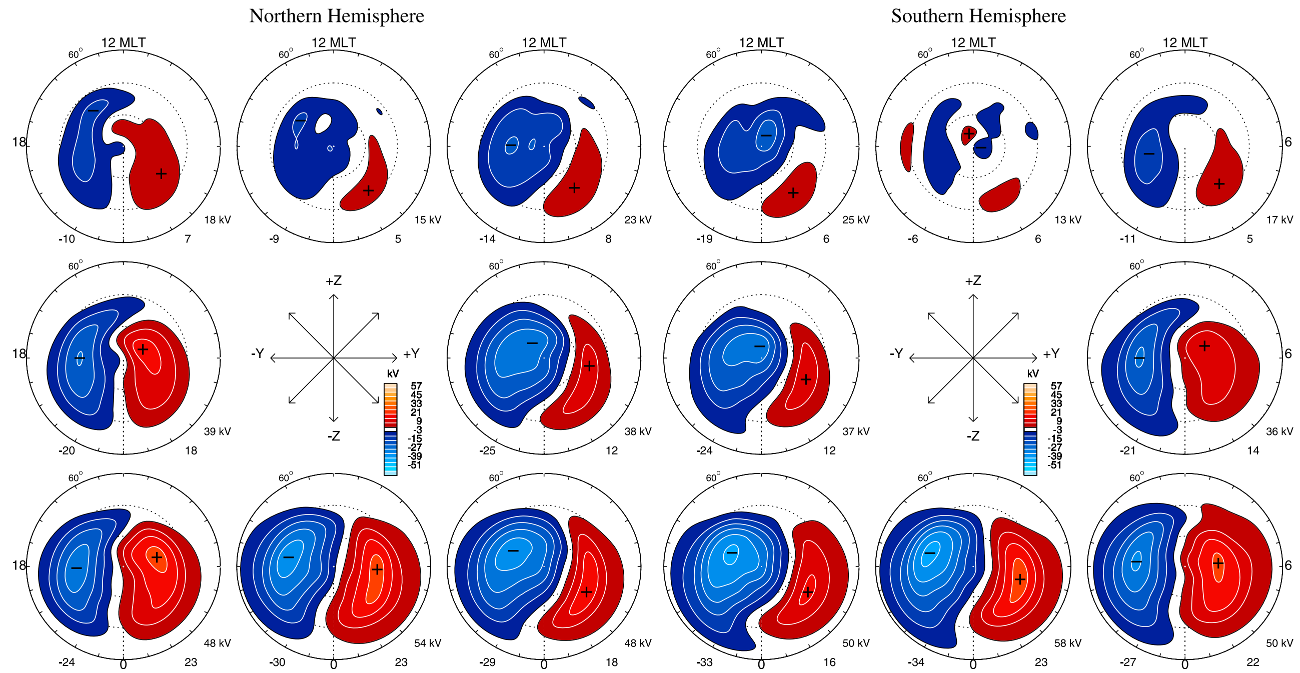

Figure 5. As for Figure 4, but for 3 nT < B_T < 5 nT.

analysis, we found that eliminating the zero padding in this region resulted in a 5% average change in the cross-polar cap potential difference (Φ_{PC}), where Φ_{PC} (hereafter referred to simply as cross-polar cap potential) is the difference between the potential maximum and minimum and is a measure of the strength of the global-scale convection. The biggest observable difference between the patterns with and without zero padding is that the lowest potential contours wander somewhat into the low-latitude dayside region.

[24] The low latitude boundary of the convection region is selected qualitatively by examining plots of the spatial distribution of backscatter rates and velocity magnitudes and selecting the boundary latitude that best aligns with the low-latitude drop-off in backscatter and velocity. The fitted solutions are to a large extent insensitive to the exact value of the boundary. Expanding the region by 4° results in at most a 5% change in Φ_{PC}, with little or no change seen in the shape or magnitude of the potential distribution at high latitudes.

3. Interhemispheric Comparisons

[25] Applying the technique described in section 2 to data obtained from the Northern and Southern hemispheres results in 72 independent convection patterns or maps for each hemisphere. Figures 4–6 show the patterns obtained for the IMF B_T = 0–3 nT, 3–5 nT, and 5–10 nT bins, respectively, for neutral tilt (<10°). The complete set of 144 patterns (including patterns for negative tilt and positive tilt) are not shown here but the figures and the spherical harmonic expansion coefficients for each map can be obtained from the author and are made available at the following URL: http://engineering.dartmouth.edu/superdarn/. Each of Figures 4–6 contains one map for each of the eight IMF clock-angle bins, arranged in clock-dial format, and this cluster is repeated for both the Northern and Southern hemispheres. Each map contains a contour plot of the electrostatic potential distribution of the fitted solution.

[26] Potential contours are shown on each map in MLT and magnetic latitude, with noon MLT at the top. For both the Northern and Southern hemispheres, dawn (6 MLT) is to the right and dusk (18 MLT) is to the left. Note that this plotting convention corresponds to a situation where all observations are viewed from above the Northern Hemisphere. That is, the Southern Hemisphere maps are plotted as though the Earth is transparent and the observation point is over the Northern Hemisphere. Although this convention may seem counter-intuitive at first, we feel that it provides the best basis for making direct comparisons of electric field patterns between hemispheres.

[27] In each map the locations of the potential maximum and minimum are indicated with a '+' sign and '−' sign, respectively. The magnitudes of these extrema, referred to as the dawn and dusk potential for the maximum and minimum, respectively, are listed at the bottom of each map. The cross polar-cap potential or transpolar potential is also shown in the lower right corner of each map.

[28] Equipotential contours are plotted at 6 kV intervals, and a color scale is provided in each cluster of eight patterns indicating the level of electrostatic potential in each map. All values of potential and potential difference are given in units of kilovolts and the scale is uniform throughout the paper.

3.1. Neutral Tilt Convection Patterns

[29] We first compare convection maps for neutral tilt, shown in Figures 4–6, because they are the most similar to those presented in RG05 for the Northern Hemisphere. In this case, the tilt angle is within 10° of zero and the geomagnetic field line topology and the solar-produced conductivity are most similar between hemispheres, thus reducing possible sources of differences. The patterns for the Northern

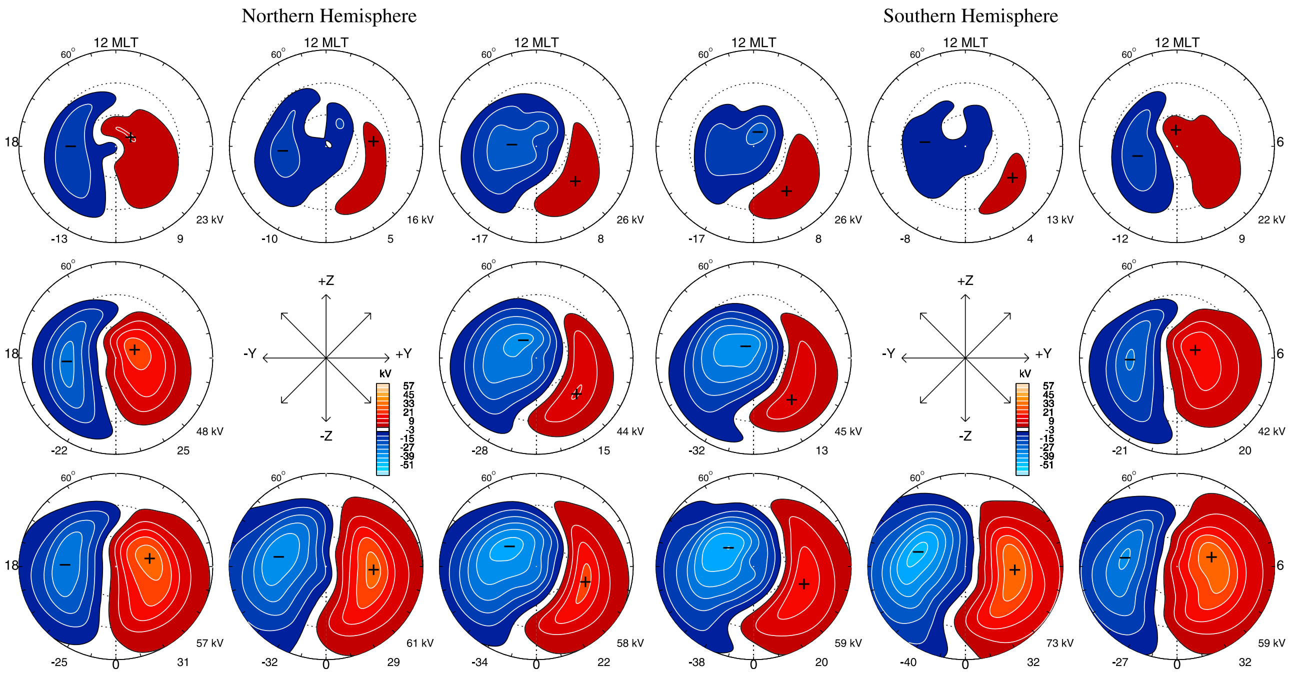

Figure 6. As for Figure 5, but for 5 nT < B_T < 10 nT.

Hemisphere closely match the patterns of RG05, with only slight differences observed which are probably the result of our secondary sorting by tilt. The patterns for the Southern Hemisphere were derived using the same technique applied to Southern Hemisphere data, and the results appear consistent with those of RG05.

[30] Figures 4–6 show that the convection patterns for the summer hemisphere are remarkably similar to those of the Northern Hemisphere. As previously shown in numerous studies [e.g., *Heppner*, 1972; *Heelis*, 1984; *Greenwald et al.*, 1990], the respective motion of newly opened flux on the dayside magnetopause with a non-zero IMF B_y results in Southern Hemisphere maps that most resemble those of the Northern Hemisphere for opposite senses of the IMF B_y component. That is, a Northern Hemisphere pattern for IMF B_y+ corresponds to a Southern Hemisphere pattern with the same conditions except for IMF B_y−. As this mirror asymmetry is already well-documented, we compare the equinoctial convection patterns of the two hemispheres after switching the sign of IMF B_y in the Southern Hemisphere.

[31] In both hemispheres, a basic two cell convection pattern is seen under all IMF clock angles other than pure northward IMF (B_z+). As the IMF clock angles increases absolutely from $\theta = 0°$ (B_z+) to $\theta = 180°$ (B_z−), the convection strength (as measured by Φ_{PC}) increases with an approximately $\sin^2(\theta/2)$ dependency in both the Northern and Southern hemispheres, peaking at $\theta = 180°$. This peak is slightly higher and sharper in the south than in the north.

[32] As the IMF orientation goes from $B_y = 0$ to pure B_y+/−, the two-cell patterns in both hemispheres are shaped into asymmetric dawn and dusk cells as expected. For B_y+ (B_y−) in the Northern (Southern) Hemisphere, the dusk cell becomes more round while the dawn cell becomes more crescent-shaped. The entire convection pattern appears rotated toward earlier MLTs. For B_y− (B_y+) in the Northern (Southern) Hemisphere, the dusk cell becomes more crescent-shaped while the dawn cell becomes more round and the pattern is rotated toward later MLTs.

[33] The convection strength in both hemispheres increases with increasing IMF magnitude. For both hemispheres, there is a bigger increase in the pattern's Φ_{PC} in the transition from the lowest magnitude bin (0–3 nT) to mid-level bin

Table 1. Φ_{PC} Values for the Northern and Southern Hemispheres, Sorted by Tilt and IMF Condition[a]

		IMF B_T Magnitude Bin					
		0–3 nT		3–5 nT		5–10 nT	
IMF	Tilt	N	S	N	S	N	S
B_z+	Negative	15	16	14	13	14	11
B_z+	Neutral	16	15	15	13	16	13
B_z+	Positive	21	–	20	–	15	18
B_z+/B_y+	Negative	20	17	22	16	26	18
B_z+/B_y+	Neutral	21	18	23	17	26	22
B_z+/B_y+	Positive	–	–	25	28	29	29
B_y+	Negative	28	23	34	29	43	34
B_y+	Neutral	30	24	38	36	44	42
B_y+	Positive	–	–	36	34	43	48
B_y+/B_z−	Negative	34	33	45	42	53	52
B_y+/B_z−	Neutral	37	32	48	50	58	59
B_y+/B_z−	Positive	39	–	45	51	50	58
B_z−	Negative	33	40	48	48	60	64
B_z−	Neutral	39	38	54	58	61	73
B_z−	Positive	–	–	53	–	64	68
B_z−/B_y−	Negative	28	34	40	42	51	47
B_z−/B_y−	Neutral	36	34	48	40	57	59
B_z−/B_y−	Positive	41	–	47	48	58	57
B_y−	Negative	23	24	29	30	36	35
B_y−	Neutral	28	29	39	37	48	45
B_y−	Positive	34	–	40	39	52	46
B_z+/B_y−	Negative	28	20	17	20	19	23
B_z+/B_y−	Neutral	20	19	18	25	23	26
B_z+/B_y−	Positive	–	–	27	26	36	29

[a]All values are given in kV. A dash (–) indicates insufficient counting statistics to completely constrain the solution.

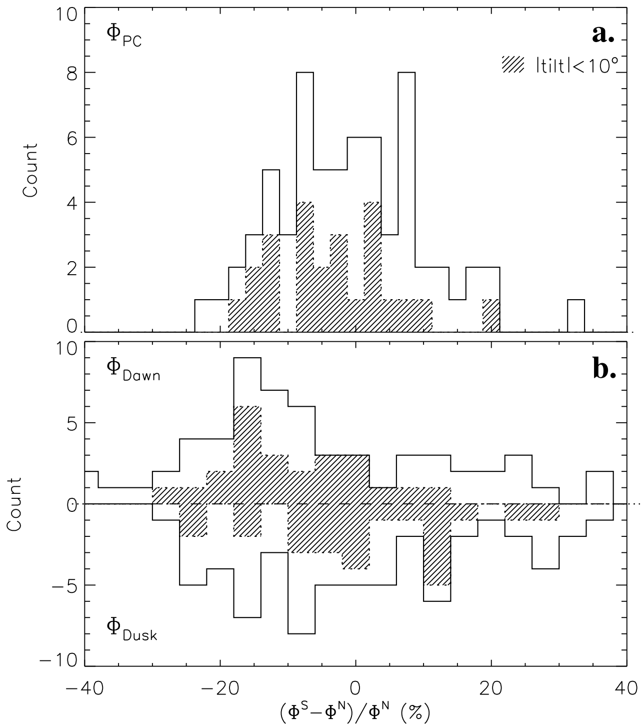

Figure 7. Distribution of the percent difference in convection parameters between the Southern and Northern hemispheres. (a) Values of the interhemispheric difference in Φ_{PC} and (b) differences in the dawn and dusk cell potentials. Interhemispheric differences in the potentials values of the neutral tilt patterns are highlighted with hatching.

(3–5 nT) than in the transition from the mid-level to highest bin (5–10 nT). The values of Φ_{PC} for all three magnitude bins are given in Table 1.

[34] The qualitative shapes of corresponding convection patterns in the Northern and Southern hemispheres are remarkably similar, often appearing to be interchangeable. To quantify this symmetry, the values of the cross-polar cap potentials, dawn and dusk cell potentials, and dawn and dusk cell locations are compared. It should be noted that, for the non-zero IMF B_y patterns, the convection patterns in the two hemispheres are derived from data obtained during different time periods since the patterns are compared under opposite signs of IMF B_y. Figure 7 shows the distribution of all the differences observed between the Southern and Northern hemispheres' Φ_{PC} values (Figure 7a) and dawn and dusk cell potential values (Figure 7b). The 72 convection patterns for all tilt and all IMF conditions from the Southern Hemisphere are compared to the 72 patterns from the Northern Hemisphere and the values of 72 differences are plotted in histogram format. A positive difference in a given parameter indicates that the Southern Hemisphere value is larger than the corresponding northern value. Interhemispheric differences in the values of the potentials of neutral tilt patterns are highlighted with hatching and are discussed in this section.

[35] Using the cross-polar cap potential, Φ_{PC}, as a global indicator of convection strength, we find that on average the absolute value of the difference between the hemispheres is 7.6% (0–12 kV). This difference is not significant compared with the average 23% change in Φ_{PC} going from one IMF magnitude bin to the next. Figure 7a shows how these interhemispheric differences in Φ_{PC} are distributed. In most cases, the differences are small (less than 5 kV) and they are randomly distributed on both sides of zero. Φ_{PC} is bigger in the Northern Hemisphere a little more than half the time, so that the average signed difference between south and north is −3.3%, but this value is considered to be negligible.

[36] The individual dawn and dusk cells are also similar between hemispheres. Comparing the northern dawn (dusk) cell to the southern dawn (dusk) cell, we find that the shapes, sizes, locations, and strengths (as measured by potential variation) of the cells are very similar.

[37] Comparing the potential variation in the individual dawn and dusk cells, we find that on average there is an 11% absolute difference in the dawn potentials and an 11% absolute difference in the dusk potentials between the two hemispheres. These are larger than the difference in Φ_{PC}. Furthermore, as seen in Figure 7b, differences in dawn cell strengths are slightly biased toward negative values (stronger in the north) while differences in dusk cell strengths are slightly biased toward positive values (stronger in the south). Because the differences are mostly anti-correlated, the differences in total Φ_{PC} are generally smaller than the individual dawn or dusk cell differences.

[38] To compare quantitatively the dawn and dusk cell locations, we consider a line drawn from the potential minimum in the dusk cell to the potential maximum in dawn cell and we measure its 'arc length' (angular separation in degrees) and rotation angle (in hours MLT, counter-clockwise from the dawn-dusk meridian) and we compare the Northern and Southern hemisphere values of these two parameters. On average, the absolute difference between the rotation angle in the two hemispheres is 0.7 hours MLT and the absolute difference in the cell separation is 2.5° latitude. These interhemispheric differences are negligible considering that the resolution of the fitted spherical harmonic expansion is 1.5 hours MLT and 4° latitude.

[39] To summarize, under neutral tilt there are some interhemispheric differences in the relative strengths of the dawn and dusk cells, but these differences are generally small and the total convection strength is very symmetric between hemispheres. The qualitative features of the convection patterns under the various IMF conditions are also very symmetric.

[40] Although the convection patterns in the two hemispheres are generally very similar there are some notable asymmetries under two particular orientations of the IMF. Under IMF B_y- (B_y+) in the north (south), Φ_{PC} is on average 12% (3.3–6.1 kV) smaller in the south than in the north. This difference is about one standard deviation greater than the average difference between south and north over all 24 equinox patterns. For this IMF orientation, the interhemispheric asymmetry is primarily located in the dawn cell; the average difference between the southern and northern dawn potential is −19% (1.7–4.5 kV). The percent differences in both the total Φ_{PC} and the dawn potentials are roughly constant over all IMF magnitude bins.

[41] Under IMF B_z-, on the other hand, Φ_{PC} is on average 8% (0–12 kV) bigger in the south than in the north. This difference is more than one standard deviation higher than

Table 2. Percent Differences Between Positive Tilt and Negative Tilt Φ_{PC} Values for the Northern and Southern Hemispheres[a]

	IMF Clock Angle Bin			
	B_z+	$B_y > 0$	$B_y < 0$	B_z-
North	30% (1–6)	4% (−3–5)	40% (7–16)	8% (4–5)
South	62% (7)	32% (5–14)	25% (5–11)	5% (3)

[a]The range of differences is given in parentheses in kV.

the overall average difference between hemispheres. In this case, the asymmetry is primarily located in the dusk cell; the average difference between the southern and northern dusk potential is +14% (1.0–8.1 kV). The percent differences in both the total Φ_{PC} and the dusk potentials grow significantly with increasing IMF magnitude.

[42] To summarize, Φ_{PC} is systematically higher in the north than south under IMF B_y- (B_y+) in the north (south) and is systematically lower in the north than south under IMF B_z-. Possible sources of these asymmetries will be discussed in section 4.

3.2. Non-zero Tilt Convection Patterns

[43] As described in section 3.1, we have found that during periods with neutral tilt the high-latitude convection is for the most part symmetric between the Northern and Southern hemispheres, with the notable exceptions being asymmetric Φ_{PC} values under IMF B_y- (B_y+) in the north (south) and under IMF B_z-. Considering convection patterns from non-zero tilt periods as well, we see that the patterns in both hemispheres exhibit a significant tilt angle dependence. Some aspects of this dependence are interhemispherically symmetric, but others are not.

[44] The response of the cross-polar cap potential to non-zero tilt is similar in both the north and south. During periods with negative tilt (tilt < −10° in the north and >10° in the south), Φ_{PC} is generally smaller than it is during neutral tilt periods for corresponding patterns, while during periods with positive tilt it is about the same or slightly larger. This trend in Φ_{PC}, however, is significantly modulated by the sign of IMF B_y; the positive tilt to negative tilt difference is greatest under $B_y < 0$ ($B_y > 0$) in the north (south). Table 2 shows the average percent difference between the positive tilt and negative tilt Φ_{PC} values for both hemispheres. Patterns where there are an insufficient number of LOS vectors to constrain the fitted solution and determine Φ_{PC} are not included in the averages; for $B_z\pm$ in the south, positive tilt Φ_{PC} values are only reliable for the 5–10 nT magnitude bin. Under $B_y > 0$ and strong (5–10 nT) IMF magnitude in the Northern Hemisphere, the negative tilt Φ_{PC} is negligibly larger (by less than 1 kV) than the positive tilt Φ_{PC}. For all IMF B_y orientations, the positive tilt to negative tilt difference increases for increasingly northward IMF.

[45] Quantitatively comparing the values of the convection pattern parameters from southern negative tilt patterns (tilt >10°) to northern negative tilt patterns (tilt < −10°) and from southern positive tilt to northern positive tilt, we find that the differences between hemispheres are similar to those observed during neutral tilt. Figure 7, discussed for neutral tilt patterns in section 3.1, shows the distribution of the interhemispheric differences in the cross-polar cap, dawn, and dusk potential values between south and north from all tilt conditions as well (unshaded histograms). For Φ_{PC} (Figure 7a), the distribution from all tilt conditions simply increases and broadens normally from the distributions for just neutral tilt periods. The overall average difference between Φ_{PC} in the south and in the north is −2.3%, which is still negligible. This behavior would be expected if the differences between hemispheres were approximately random and Gaussian, since including all tilt conditions adds more data samples. These unbiased, random differences match the previous observation that both hemispheres' Φ_{PC} vary with tilt in a similar fashion.

[46] While the dependence of Φ_{PC} on tilt is similar between hemispheres, with any interhemispherical differences being small compared to the large variations from one tilt condition to the next, the dawn and dusk cells' response to non-zero tilt is interhemispherically asymmetric. For negative tilt patterns, the ratio of dusk to dawn potentials is smaller in the south than in the north. Stated differently, the dawn cell is generally stronger in the south than in the north while the dusk cell is generally weaker. For positive tilt patterns, these relationships are reversed. The south has a larger dusk-to-dawn potential ratio than the north, corresponding to a weaker dawn cell and stronger dusk cell in the south than in the north. Since the individual dawn and dusk cells respond to changing tilt differently in the Northern and Southern hemispheres, the interhemispheric differences are not expected to be random and unbiased. As seen in Figure 7b, the shapes of the distributions of differences change when all tilt conditions, not just neutral tilt, are included. Additionally, if all tilt conditions are included, the average absolute difference between the two hemispheres' dawn potentials and between their dusk potentials is 20% and 15% respectively, much larger than the corresponding differences in neutral tilt patterns.

[47] To obtain a rough estimate of the uncertainty in the cross-polar cap, dawn, and dusk potential values which are being compared, we select four patterns from each tilt angle condition (12 total patterns per hemisphere) and randomly divide the raw data from each pattern into two subsets. The binning, averaging, and fitting procedure is performed independently on the two subsets of data, and the resulting cross-polar cap, dawn, and dusk potential values are compared. The average variation in Φ_{PC} between the subsets is 1.8% (3.0%) in the north (south), similar to the average difference of −2.3% between hemispheres, which is considered negligible. The average variation in the values of the dawn and dusk potentials is 2.2% (4.1%) in the north (south), which is much smaller than the average difference in the values between the hemispheres. The uncertainty in the value of Φ_{PC} is also much smaller than the difference between its values for positive tilt and for negative tilt, discussed previously in section 3.2 and shown in Table 2.

[48] These dawn and dusk cell asymmetries can be better understood by considering the development of each hemisphere's convection patterns individually as tilt angle progresses from negative tilt to neutral tilt to positive tilt. Figure 8 shows the patterns for IMF B_y+/− in the 5–10 nT magnitude bin for all three tilt conditions in both hemispheres. We focus mainly on the patterns from these particular IMF conditions in order to identify the primary effects that tilt has on convection. We have selected the IMF B_y+/−, IMF $B_z = 0$ patterns because they have been previ-

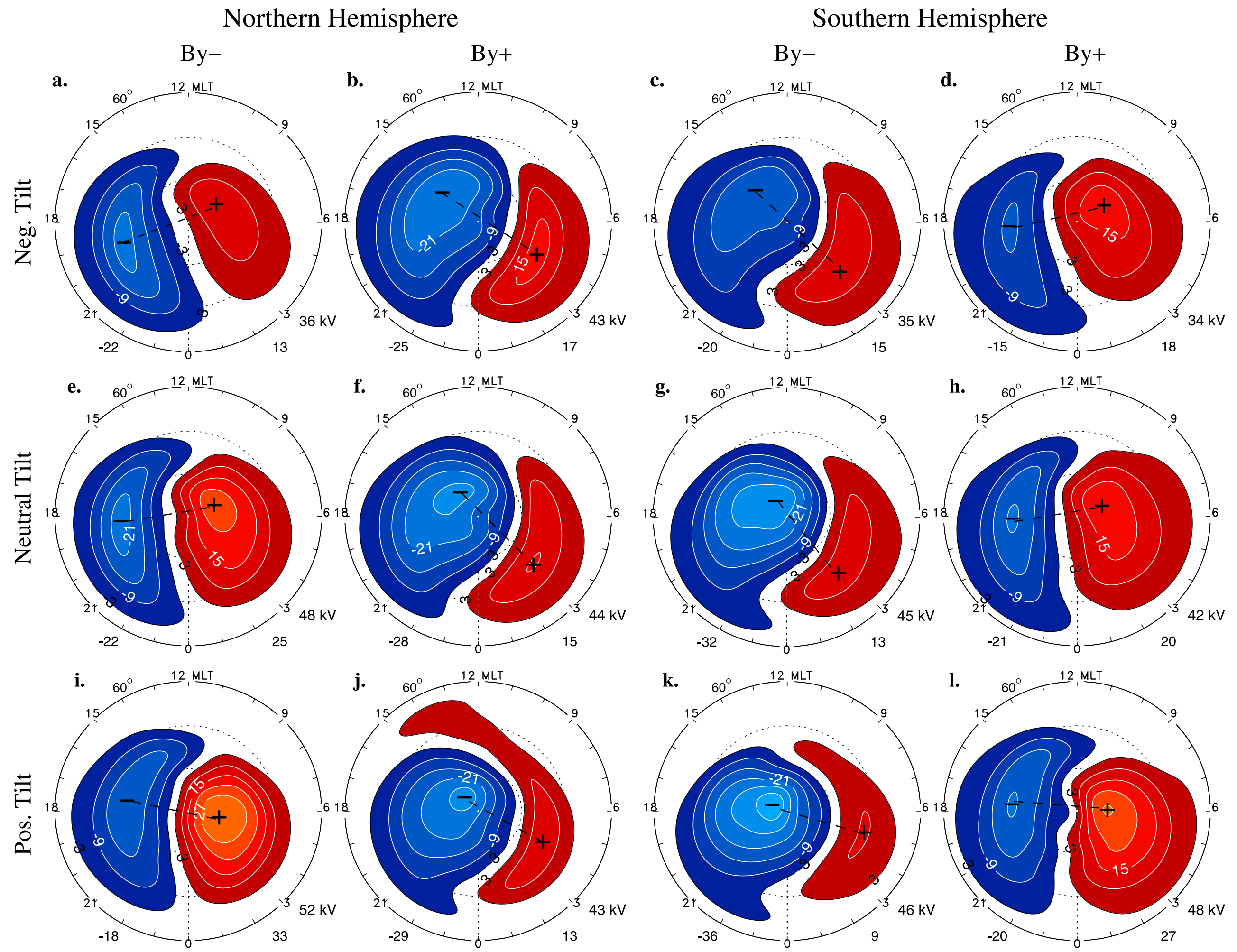

Figure 8. Statistical convection patterns sorted by tilt. IMF B_y+/−, 5 nT < B_T < 10 nT.

ously studied in reconnection theory [e.g., *Crooker and Rich*, 1993]. Additionally, in our analyses, these patterns contain the most data (see Figure 2) and they exhibit the most systematic variations with changing tilt.

[49] In the north, under IMF B_y+, little change is seen in the pattern as tilt increases. These patterns are shown in Figures 8b, 8f, and 8j. During periods with positive tilt, the round dusk cell is slightly enhanced while the crescent dawn cell is slightly weakened. Under IMF B_y− (Figures 8a, 8e, and 8i), however, the round dawn cell grows significantly with increasing tilt, especially in the step from negative tilt to neutral tilt. The crescent dusk cell gets weaker and the whole pattern rotates towards earlier MLTs as tilt increases. This dependency, which is much more pronounced under IMF B_y− than B_y+, is very similar to that shown in RG05, even though true season rather than dipole tilt was used to sort the data in RG05.

[50] A different development is seen in the south. Patterns from IMF B_y− are shown in Figures 8c, 8g, and 8k, which is the conjugate of IMF B_y+ in the north (Figures 8b, 8f, and 8j). For this IMF orientation, the round dusk cell grows significantly as tilt increases, especially in the step from negative tilt to neutral tilt. The crescent dawn cell gets weaker with each step in tilt, and under positive tilt the whole pattern rotates towards later MLTs. For IMF B_y+ (Figures 8d, 8h, and 8l, the conjugate of Figures 8a, 8e, and 8i), less change is observed. The whole pattern is enhanced in the step from negative tilt to neutral tilt, and the round dawn cell is enhanced while the crescent dusk cell is slightly weakened in the step from neutral tilt to positive tilt. The pattern rotates towards earlier MLTs as tilt increases.

[51] The patterns for IMF B_y+/− with non-zero IMF B_z show similar development with increasing tilt (not shown here). Table 1 shows the values of Φ_{PC} for all tilt and IMF conditions.

[52] While the IMF B_y+/− patterns exhibit the greatest asymmetries between hemispheres, the most interhemispherically symmetric development with increasing tilt is seen in the B_z+ patterns, shown in Figure 9 for the 5–10 nT IMF magnitude bin. Under negative tilt (Figure 9a), convection is limited to a single weak cell, with the return flow occurring almost exclusively on the dusk side. A pair of small reverse convection cells is seen at very high latitudes on the dayside, contained within the larger single-cell. These are more visible in a map of the velocity vectors (not shown). Under neutral tilt (Figure 9b), the patch of reverse convection grows in both size and strength, extending to slightly lower latitudes. It appears to be superimposed on a

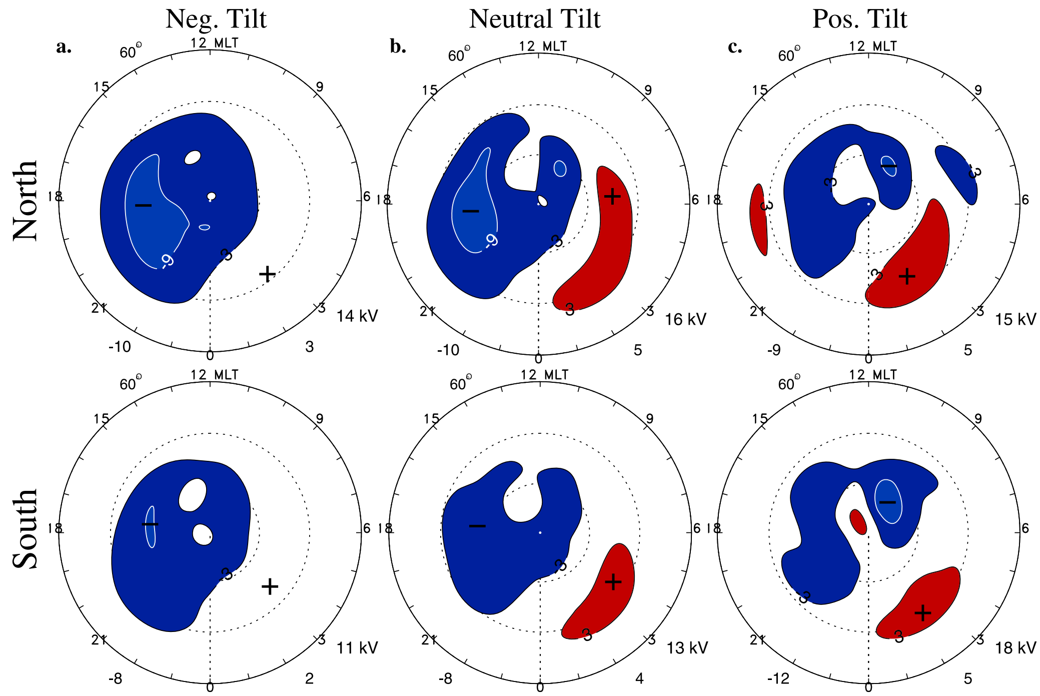

Figure 9. Statistical convection patterns sorted by tilt. IMF B_z+, 5 nT < B_T < 10 nT.

weak two-cell pattern. Under positive tilt (Figure 9c), the reverse convection grows significantly, extending somewhat to the nightside at high latitudes. The two cell pattern is only observed in the lower latitudes on the nightside.

4. Discussion

[53] Overall, the differences in the convection patterns in the Northern and Southern hemispheres are small with the exceptions of a higher southern than northern Φ_{PC} under IMF B_z− and the asymmetric dawn and dusk cells, particularly under IMF B_y+/−, which seem to be related to an asymmetric dependence on dipole tilt. We therefore first consider possible causes of the observed dependence of the convection patterns on dipole tilt. We then discuss the interhemispherical asymmetries and their possible relationship to dipole tilt or other effects.

4.1. Tilt Effects

[54] The discussion of tilt effects are divided into those associated with northward IMF and those associated with IMF B_y.

4.1.1. Northward IMF (B_z+; B_y = 0)

[55] Under northward IMF (B_z+), the development of the convection patterns with increasing tilt (winter-like to summer-like) is most symmetric between the hemispheres. The appearance and growth of a patch of reverse convection at high latitudes is consistent with the effects of an overdraped lobe cell as described by *Crooker and Rich* [1993]. As the tilt angle increases, the rate of reconnection with the tail lobe grows and the strength of the lobe cell circulation grows.

[56] The existence of reverse convection cells under negative tilt could be the result of a merging topology as described by *Watanabe et al.* [2005] that produces "reciprocal cells" in the winter hemisphere (mostly negative tilts) in addition to lobe cells in the summer hemisphere (mostly positive tilts). Observations of lobe reconnection in both hemispheres during northern winter were also reported in a case study by *Marcucci et al.* [2008].

[57] For neutral tilt, our results show lobe-cell-like convection in both hemispheres (Figure 9b). This result could be due to the inclusion of data from time periods with both slightly positive and slightly negative tilts (|tilt| <10°), with lobe cells being generated in only one hemisphere at any given time. Alternatively, lobe-cell-like convection under neutral tilt could be a signature of dual lobe reconnection, which causes reverse convection in both hemispheres simultaneously as seen in a case study by *Imber et al.* [2007].

4.1.2. IMF B_y+ and B_y− (Any B_z)

[58] The development of the B_y+ and B_y− convection patterns with increasing tilt is more complex and less symmetric between hemispheres. In particular, there appears to be a different behavior when patterns from negative and neutral tilts are compared and when patterns from neutral and positive tilts (equinox-like to summer-like) are compared. In the former case (winter-like to equinox-like), both hemispheres respond similarly for IMF B_y < 0, with the round, dawn (dusk) cell being enhanced by ~10 kV in the Northern (Southern) Hemisphere (e.g., Figures 8a and 8e and Figures 8c and 8g). In the latter case (equinox-like to summer-like), patterns in either hemisphere seem to respond similarly for opposite signs of IMF B_y. For instance, under IMF B_y < 0 (B_y > 0) in the Northern (Southern) Hemisphere the potential in the round dawn cell increases by 3 to 12 kV (e.g., Figures 8e and 8i and Figures 8h and 8l), while under IMF B_y > 0 (B_y < 0) the potential in the round dusk cell increases by at most a few kilovolts (e.g., Figures 8f and 8j

and Figures 8g and 8k). Larger enhancements generally occur with increasingly northward IMF.

[59] There is no simple explanation for the observed difference in the behavior of the patterns with increasing tilt. One possible cause of the enhanced round cell with increasing tilt is the presence of an overdraped lobe cell, similar to that observed under northward IMF. However, this scenario does not explain why in the case of negative to neutral tilt the observed enhancement occurs for the same sign of IMF B_y, not the opposite sign, as would be expected with the new antiparallel merging topology. Another possible explanation is enhanced dayside reconnection for increasing tilt, although why the enhancement would depend differently on the hemisphere and the sign of IMF B_y is not clear.

[60] Another change associated with non-zero IMF B_y that occurs with increasing tilt is a change in the potential of the round cell relative to the crescent cell. The shaping of the cells and the potential variations reinforce the dominance of the dusk cell when IMF B_y is positive (negative) in the north (south) but weakens it when IMF B_y is negative (positive).

[61] This behavior is often, but not always, accompanied by a rotation of the pattern in MLT toward the side occupied by the round cell, i.e. towards dawn if IMF B_y is negative (positive) in the north (south). The sense of rotation is opposed to that of the rotation occurring due to the IMF B_y effect. For example, Figures 8a, 8e, and 8i show a rotation of the line drawn between the potential extrema to earlier MLTs. In this case, the typical rotation to later MLTs that occurs under IMF B_y- is 'canceled out' and the line between the potential extrema is approximately aligned with the dawn-dusk meridian. A similar result was noted by RG05 for the Northern Hemisphere, in which the combination of IMF B_y+ and summer was observed to 'reinforce' the IMF B_y effect while the IMF B_y-/summer combination was found to be 'non-reinforcing'.

[62] In addition, a similar variation in the morphology of the convection patterns was also noted by *Zhang et al.* [2007] and *de la Beaujardière et al.* [1991] and was attributed to the day-night conductivity gradient, which shifts antisunward as season progresses from winter (mostly negative tilt) to summer (mostly positive tilt). *Zhang et al.* [2007] describes the motion of the cells as an antisunward shift that was more significant in the dawn cell than the dusk cell, resulting in an apparent rotation towards earlier MLTs for both signs of IMF B_y. In our patterns, the round cell's antisunward shift is larger than the crescent-shaped cell under both signs of IMF B_y, resulting in a rotation towards later MLTs for IMF B_y+ (B_y-) in the north (south).

[63] It is possible that the decrease in the strength of the crescent-shaped cell is the result of conductivity increasing with increasing tilt angle. To the extent that the M-I coupling can be described as a current source, when conductance increases, potential decreases. In an MHD modeling study, *Ridley et al.* [2004] found that increasing the Hall and Pedersen conductances in the ionosphere, mimicking summer conditions, decreased the potential values significantly. In our results, a decrease is seen in the crescent-shaped cell, while an increase is seen in the round cell, possibly due to a dominating effect of lobe cell generation in the round cell.

[64] For IMF B_y+ (B_y-) in the north (south), the enhanced round cell is located in the dusk sector so that, as noted by *Zhang et al.* [2007], *Weimer* [1995], and *Crooker and Rich* [1993], the dusk and dawn potentials are most different for this sign of azimuthal IMF in the summer (or under positive tilt). While for IMF B_y- (B_y+) in the north (south), the round cell is located at dawn and our patterns show that not only does the dawn cell contain as much potential variation as the dusk cell, as described by *Zhang et al.* [2007], *Weimer* [1995], and *Crooker and Rich* [1993], it actually surpasses the dusk cell.

[65] The contrasting effects on the round and crescent cells combine to result in the Φ_{PC} dependence on tilt described in section 3.2. Under most IMF orientations, Φ_{PC} is larger for positive tilt than for negative tilt but there is little difference in Φ_{PC} for different tilt angles under IMF B_y+ in the north, when the diminishing crescent cell and the weak lobe cell generation balance each other, and under IMF B_z- in both hemispheres, when lobe cell generation does not seem to occur.

[66] Previous studies such as *Papitashvili and Rich* [2002], *Weimer* [2005], and *de la Beaujardière et al.* [1991] have found positive tilt cross-polar cap potentials to be generally similar to or smaller than negative tilt potentials. However, the combined effect of tilt angle and IMF clock angle described here is similar to that found in many other studies. *Papitashvili and Rich* [2002] reported higher summer than winter potentials for the particular IMF orientations B_y- and B_z+. The model of *Weimer* [1995] gives higher positive tilt than negative tilt potentials for IMF $B_y < 0$, for IMF B_z+, and for some cases of IMF $B_y > 0$. *Zhang et al.* [2007] also shows higher potentials in the summer if IMF B_y is negative and in the winter if IMF B_y is positive. In several case studies, *Lu et al.* [1994] found that Φ_{PC} in the summer hemisphere was much larger than Φ_{PC} in the winter hemisphere for IMF B_y- and B_z+.

[67] Note that we have assumed that the tilt angle dependencies observed in our results are due to the effects of different dipole tilt angles and not due to effects of true geophysical season. To test this assumption, we sort data for the highest IMF magnitude bin (5–10 nT), IMF $B_y+/-$ patterns by both dipole tilt and true season (as determined by day-of-year). Using only periods whose dipole tilt angle magnitude is <10° (neutral tilt), a secondary sorting into summer season data and winter season data was performed and the resulting seasonal convection patterns were found to be similar in morphologies and in cross-polar cap potential values. Conversely, using data from equinoctial time periods only (within ±45 days of the spring or fall equinox), the convection patterns derived from a secondary sorting into negative tilt periods (tilt < −10°) and positive tilt periods (tilt >10°) were compared. In this case, there were significant differences in the morphologies and potential values. Because a greater variation is observed in the patterns sorted by dipole tilt rather than by season–presumably since the dipole tilt is a more accurate measure of the Earth's magnetic field geometry and of the amount of solar-produced ionospheric conductivity (possible causes of the observed dependence)–it seems appropriate to use the dipole tilt angle to sort our convection patterns.

4.2. Interhemispheric Asymmetries

[68] After considering dipole tilt effects, it is evident that the asymmetry in the cross-polar cap potentials of the hemispheres under IMF B_y- (B_y+) in the north (south) during neutral tilt (described in section 3.1) is consistent with asymmetric lobe cell generation which occurs preferentially under IMF B_y- in both hemispheres. Since this enhancement occurs in both hemispheres under the same sign of IMF B_y, when the hemispheres are compared under opposite signs of IMF B_y, the enhanced hemisphere's Φ_{PC} is larger, in this case the Northern Hemisphere. As noted before, differences in the potentials of the round dawn cell were the primary source of the difference in Φ_{PC} between hemispheres, and for this sign of IMF B_y the lobe cell is added to this round cell, enhancing its potential. This asymmetry in Φ_{PC} persists for positive tilt periods as well, although the difference between hemispheres is smaller. A similar but weaker effect is seen under IMF B_y+ (B_y-) in the north (south) during positive tilt. In this case, the Southern (B_y-) Hemisphere has the strong lobe cell so its Φ_{PC} is slightly greater than that of the Northern Hemisphere.

[69] The asymmetry in the hemispheres' Φ_{PC} under IMF B_z- also remains an outstanding question. For this IMF orientation, even averaging over all tilt angles and all IMF magnitude bins, Φ_{PC} in the south is 6.5% (0–12 kV) larger than Φ_{PC} in the north. This difference is about one standard deviation above the overall mean of −2.3% difference between Φ_{PC} in the south and Φ_{PC} in the north. A similar interhemispheric asymmetry under IMF B_z- is observed by *Papitashvili and Rich* [2002].

[70] This asymmetry could be the result of data biases such as differences in the number or spatial distribution of velocity measurements, but this is unlikely. As shown in Figure 3, the distribution of velocity data is similar in both hemispheres. Although there is approximately a factor of 2 difference between the number of LOS measurements in the north and south, if the data in the Northern Hemisphere is artificially decimated to better match the Southern Hemisphere, it must be decreased by a factor of 32 to achieve a 6% increase in Φ_{PC}. Furthermore, a similar factor of 2 difference between the amount of data in the north and south persists for all IMF conditions but only under IMF B_z- is the southern Φ_{PC} systematically larger than the northern Φ_{PC}.

[71] The non-dipolar, asymmetric nature of the Earth's magnetic field could also play a role. Because the Earth's field is not a true dipole, the mapping of locations (and velocities) from geographic to geomagnetic coordinates is non-uniform and asymmetric across hemispheres, possibly introducing asymmetric errors in the calculation of electric potential values in geomagnetic coordinates if the non-uniformities are not taken into account [*Gasda and Richmond*, 1998]. Also, unequal field strengths due, for example, to the South Atlantic Anomaly and different magnetic pole offsets, which result in a difference in the relative location of the terminator, might cause differences in the strength of convection observed in the two hemispheres.

5. Summary

[72] Using five years of SuperDARN line-of-sight velocity data collected independently in the Northern and Southern hemispheres, a standard technique has been used to derive climatological models of convection for both hemispheres, parameterized by both the IMF condition and the dipole tilt angle.

[73] We have found that dipole tilt angle has a significant effect on the convection patterns of both hemispheres, possibly due to changing reconnection topologies and solar produced conductivities. This parameter was missing from the previous SuperDARN models (RG96 and RG05) but is an easy dependence to include as so much data is available that the additional sorting generally leaves enough data in each model bin such that the LOS vectors constrain the fitted solution across the entire magnetic latitude, MLT grid.

[74] As found in previous studies, our results show that the dependence of the convection pattern on tilt is strongly modulated by the IMF clock angle. During northward or B_y dominated IMF, convection under positive tilt is enhanced compared to convection under negative tilt, consistent with the generation of lobe cells. The lobe cell causes reverse convection during pure northward IMF but is added to the round-shaped merging cell during periods of non-zero IMF B_y. Lobe cell generation is observed to be strongest during IMF $B_y < 0$ in both hemispheres and weakest during IMF $B_y > 0$ in the Northern Hemisphere. The origin of this asymmetric dependence on the sense of IMF B_y is unaccounted for.

[75] The crescent-shaped merging cell, on the other hand, weakens as tilt angle increases, possibly due to conductivity differences between the negative tilt and positive tilt hemispheres. This, however, is not the dominant effect in our results and as a result, the cross-polar cap potentials under positive tilt ('summer') are generally higher than the potentials under negative tilt ('winter'), possibly due to a dominating effect of lobe cell generation.

[76] Comparing hemispheres, we find that, qualitatively, the Northern and Southern hemispheres are very symmetric, even during periods with non-zero tilt. Quantitatively, Φ_{PC} is generally symmetric between hemispheres, except for during IMF B_z- for all tilts, when Φ_{PC} is systematically larger in the south than in the north, or during B_y- (B_y+) in the north (south) under neutral tilt, when Φ_{PC} is larger in the north. The dawn and dusk potentials vary more with tilt than does Φ_{PC} and they are more interhemispherically asymmetric.

[77] It should also be noted that all of our interhemispherical comparisons have been performed after changing the sign of both IMF B_y and the dipole tilt in the Southern Hemisphere. If the hemispheres are compared simultaneously, significant differences can be observed if there is a strong IMF B_y component or a non-zero dipole tilt, such as in the case studies by *Knipp et al.* [1993, 2000] and *Lu et al.* [1994].

[78] Although neutral tilt patterns are similar enough to be used interchangeably, convection has a strong dipole tilt angle dependence and a Northern Hemisphere convection model should not be applied to the Southern Hemisphere if dipole tilt is not taken into account. Even when dipole tilt is accounted for, while Φ_{PC} differs between hemispheres by less than 10% on average, the strength of the convection in the individual cells differs by 15% to 20% on average.

[79] **Acknowledgments.** Operation of the SuperDARN radars is supported by the national funding agencies of the U.S., Canada, the U.K., France, Japan, Italy, South Africa, and Australia. We gratefully acknowl-

edge the ACE/MAG instrument team, the ACE/SWEPAM instrument team, and the CDAWeb for providing the ACE level 2 data used in this study. This work was supported by NSF grants ATM-0836485 and ATM-0838356, and NASA grant NNG-05667H.

[80] Robert Lysak thanks Steven Morley and another reviewer for their assistance in evaluating this paper.

References

Boyle, C. B., P. H. Reiff, and M. R. Hairston (1997), Empirical polar cap potentials, *J. Geophys. Res.*, *102*, 111.

Bristow, W. A., and P. Jensen (2007), A superposed epoch study of SuperDARN convection observations during substorms, *J. Geophys. Res.*, *112*, A06232, doi:10.1029/2006JA012049.

Chisham, G., et al. (2007), A decade of the Super Dual Auroral Radar Network (SuperDARN): Scientific achievements, new techniques and future directions, *Surv. Geophys.*, *28*, 33.

Codrescu, M. V., T. J. Fuller-Rowell, and J. C. Foster (1995), On the importance of E-field variability for Joule heating in the high-latitude thermosphere, *Geophys. Res. Lett.*, *22*, 2393.

Codrescu, M. V., T. J. Fuller-Rowell, J. C. Foster, J. M. Holt, and S. J. Cariglia (2000), Electric field variability associated with the Millstone Hill electric field model, *J. Geophys. Res.*, *105*, 5265.

Cowley, S. W. H. (1982), The causes of convection in the Earth's magnetosphere—A review of developments during the IMS, *Rev. Geophys.*, *20*, 531.

Cowley, S. W. H., and M. Lockwood (1992), Excitation and decay of solar wind-driven flows in the magnetosphere-ionosphere system, *Ann. Geophys.*, *10*, 103.

Crooker, N. U., and F. J. Rich (1993), Lobe cell convection as a summer phenomenon, *J. Geophys. Res.*, *98*, 13,403.

Crowley, G., and C. L. Hackert (2001), Quantification of high latitude electric field variability, *Geophys. Res. Lett.*, *28*, 2783.

de la Beaujardière, O., D. Alcaydé, J. Fontanari, and C. Leger (1991), Seasonal dependence of high-latitude electric fields, *J. Geophys. Res.*, *96*, 5723.

Fedder, J. A., and J. G. Lyon (1987), The solar wind-magnetosphere-ionosphere current-voltage relationship, *Geophys. Res. Lett.*, *14*, 880.

Fedder, J. A., C. M. Mobarry, and J. G. Lyon (1991), Reconnection voltage as a function of IMF clock angle, *Geophys. Res. Lett.*, *18*, 1047.

Foster, J. C., J. M. Holt, R. G. Musgrove, and D. S. Evans (1986), Ionospheric convection associated with discrete levels of particle precipitation, *Geophys. Res. Lett.*, *13*, 656.

Fuller-Rowell, T. J., D. Rees, S. Quegan, R. J. Moffett, M. V. Codrescu, and G. H. Millward (1996), A coupled thermosphere-ionosphere CTIM, in *STEP Handbook of Ionospheric Models*, edited by R. W. Schunk, p. 217, Sci. Comm. on Sol. Terr. Phys., NOAA, Boulder, Colo.

Gasda, S., and A. D. Richmond (1998), Longitudinal and interhemispheric variations of auroral ionospheric electrodynamics in a realistic geomagnetic field, *J. Geophys. Res.*, *103*, 4011.

Gillies, R. G., G. C. Hussey, G. J. Sofko, K. A. McWilliams, R. A. D. Fiori, P. Ponomarenko, and J.-P. St.-Maurice (2009), Improvement of SuperDARN velocity measurements by estimating the index of refraction in the scattering region using interferometry, *J. Geophys. Res.*, *114*, A07305, doi:10.1029/2008JA013967.

Greenwald, R. A., K. B. Baker, J. M. Ruohoniemi, J. R. Dudeney, M. Pinnock, N. Mattin, J. M. Leonard, and R. P. Lepping (1990), Simulataneous conjugate observations of dynamic variations in high-latitude dayside convection due to changes in IMF B_y, *J. Geophys. Res.*, *95*, 8057.

Heelis, R. A. (1984), The effects of interplanetary magnetic field orientation on dayside high latitude ionospheric convection, *J. Geophys. Res.*, *89*, 2873.

Heppner, J. P. (1972), Polar-cap electric field distributions related to the interplanetary magnetic field direction, *J. Geophys. Res.*, *77*, 4877.

Heppner, J. P. (1977), Empirical models of high-latitude electric fields, *J. Geophys. Res.*, *82*, 1115.

Heppner, J. P., and N. C. Maynard (1987), Empirical high-latitude electric field models, *J. Geophys. Res.*, *92*, 4467.

Holt, J. M., R. H. Wand, J. V. Evans, and W. L. Oliver (1987), Empirical models for the plasma convection at high latitudes from Millstone Hill observations, *J. Geophys. Res.*, *92*, 203.

Imber, S. M., S. E. Milan, and B. Hubert (2007), Observations of significant flux closure by dual lobe reconnection, *Ann. Geophys.*, *25*, 1617.

Knipp, D. J., et al. (1993), Ionospheric convection response to slow, strong variations in a northward interplanetary magnetic field: A case study for January 14, 1988, *J. Geophys. Res.*, *98*, 19,273.

Knipp, D. J., C.-H. Lin, B. A. Emery, J. M. Ruohoniemi, F. J. Rich, and D. S. Evans (2000), Hemispheric asymmetries in ionospheric electrodynamics during the solar wind void of 11 May 1999, *Geophys. Res. Lett.*, *27*, 4013.

Koustov, A. V., G. J. Sofko, D. André, D. W. Danskin, and L. V. Benkevitch (2004), Seasonal variation of HF radar F region echo occurrence in the midnight sector, *J. Geophys. Res.*, *109*, A06305, doi:10.1029/2003JA010337.

Lester, M., S. E. Milan, G. Provan, and J. A. Wild (2006), Review of ionospheric effects of solar wind magnetosphere coupling in the context of the expanding contracting polar cap boundary model, *Space Sci. Rev.*, *124*, 117.

Lu, G., P. H. Reiff, M. R. Hairston, R. A. Heelis, and J. L. Karty (1989), Distribution of convection potential around the polar cap boundary as a function of the interplanetary magnetic field, *J. Geophys. Res.*, *94*, 13,447.

Lu, G., et al. (1994), Interhemispheric asymmetry of the high-latitude ionospheric convection pattern, *J. Geophys. Res.*, *99*, 6491.

Lukianova, R., C. Hanuise, and F. Christiansen (2008), Asymmetric distribution of the ionospheric electric potential in the opposite hemispheres as inferred from the SuperDARN observations and FAC-based convection model, *J. Atmos. Sol.-Terr. Phys.*, *70*, 2324.

Mandea, M., and S. Macmillan (2000), International Geomagnetic Reference Field—The eighth generation, *Earth Planets Space*, *52*, 1119.

Marcucci, M. F., I. Coco, D. Ambrosino, E. Amata, S. E. Milan, M. B. Bavassano Cattaneo, and A. Retinò (2008), Extended SuperDARN and IMAGE observations for northward IMF: Evidence for dual lobe reconnection, *J. Geophys. Res.*, *113*, A02204, doi:10.1029/2007JA012466.

Matsuo, T., A. D. Richmond, and K. Hensel (2003), High-latitude ionospheric electric field variability and electric potential derived from DE-2 plasma drift measurements: Dependence on IMF and dipole tilt, *J. Geophys. Res.*, *108*(A1), 1005, doi:10.1029/2002JA009429.

Papitashvili, V. O., and F. J. Rich (2002), High-latitude ionospheric convection models derived from Defense Meteorological Satellite Program ion drift observations and parameterized by the interplanetary magnetic field strength and direction, *J. Geophys. Res.*, *107*(A8), 1198, doi:10.1029/2001JA000264.

Papitashvili, V. O., B. A. Belov, D. S. Faermark, Y. I. Feldstein, S. A. Golyshev, L. I. Gromova, and A. E. Levitin (1994), Electric potential patterns in the northern and southern polar regions parameterized by the interplanetary magnetic field, *J. Geophys. Res.*, *99*, 13,251.

Papitashvili, V. O., F. J. Rich, M. A. Heinemann, and M. R. Hairston (1999), Parameterization of the Defense Meteorological Satellite Program ionospheric electrostatic potentials by the interplanetary magnetic field strength and direction, *J. Geophys. Res.*, *104*, 177.

Reiff, P. H., R. W. Spiro, and T. W. Hill (1981), Dependence of polar cap potential drop on interplanetary parameters, *J. Geophys. Res.*, *86*, 7639.

Rich, F. J., and M. Hairston (1994), Large-scale convection patterns observed by DMSP, *J. Geophys. Res.*, *99*, 3827.

Richmond, A. D., and Y. Kamide (1988), Mapping electrodynamic features of the high-latitude ionosphere from localized observations: Technique, *J. Geophys. Res.*, *93*, 5741.

Ridley, A. J. (2005), A new formulation for the ionospheric cross polar cap potential including saturation effects, *Ann. Geophys.*, *23*, 3533.

Ridley, A. J., T. I. Gombosi, and D. L. DeZeeuw (2004), Ionospheric control of the magnetosphere: Conductance, *Ann. Geophys.*, *22*, 567.

Ridley, A. J., Y. Deng, and G. Tóth (2006), The global ionosphere-thermosphere model, *J. Atmos. Sol.-Terr. Phys.*, *68*, 839.

Ruohoniemi, J. M., and K. B. Baker (1998), Large-scale imaging of high-latitude convection with Super Dual Auroral Radar Network HF radar observations, *J. Geophys. Res.*, *103*, 20,797.

Ruohoniemi, J. M., and R. A. Greenwald (1996), Statistical patterns of high-latitude convection obtained from Goose Bay HF radar observations, *J. Geophys. Res.*, *101*, 21,743.

Ruohoniemi, J. M., and R. A. Greenwald (1997), Rates of scattering occurrence in routine HF radar observations during solar cycle maximum, *Radio Sci.*, *32*, 1051.

Ruohoniemi, J. M., and R. A. Greenwald (1998), The response of high-latitude convection to a sudden southward IMF turning, *Geophys. Res. Lett.*, *25*, 2913.

Ruohoniemi, J. M., and R. A. Greenwald (2005), Dependencies of high-latitude plasma convection: Consideration of interplanetary magnetic field, seasonal, and universal time factors in statistical patterns, *J. Geophys. Res.*, *110*, A09204, doi:10.1029/2004JA010815.

Ruohoniemi, J. M., S. G. Shepherd, and R. A. Greenwald (2002), The response of the high-latitude ionosphere to IMF variations, *J. Atmos. Sol.-Terr. Phys.*, *64*, 159.

Schunk, R. W., et al. (2004), Global Assimilation of Ionospheric Measurements (GAIM), *Radio Sci.*, *39*, RS1S02, doi:10.1029/2002RS002794.

Shepherd, S. G., and J. M. Ruohoniemi (2000), Electrostatic potential patterns in the high latitude ionosphere constrained by SuperDARN measurements, *J. Geophys. Res.*, *105*, 23,005.

Shepherd, S. G., and F. Shubitidze (2003), Method of auxiliary sources for calculating the magnetic and electric fields induced in a layered Earth, *J. Atmos. Sol.-Terr. Phys.*, *65*(10), 1151–1160.

Shepherd, S. G., J. M. Ruohoniemi, and R. A. Greenwald (2003), Direct measurements of the ionospheric convection variability near the cusp/throat, *Geophys. Res. Lett.*, *30*(21), 2109, doi:10.1029/2003GL017668.

Siscoe, G. L., and T. S. Huang (1985), Polar cap inflation and deflation, *J. Geophys. Res.*, *90*, 543.

Tanaka, Y., M. Hayakawa, and M. Nishino (2001), Interplanetary magnetic field B_y and auroral conductance effects on high-latitude ionospheric convection patterns, *J. Geophys. Res.*, *106*, 24,505.

Watanabe, M., K. Kabin, G. J. Sofko, R. Rankin, T. I. Gombosi, A. J. Ridley, and C. R. Clauer (2005), Internal reconnection for northward interplanetary magnetic field, *J. Geophys. Res.*, *110*, A06210, doi:10.1029/2004JA010832.

Watanabe, M., G. J. Sofko, K. Kabin, R. Rankin, A. J. Ridley, C. R. Clauer, and T. I. Gombosi (2007), Origin of the interhemispheric potential mismatch of merging cells for interplanetary magnetic field B_Y-dominated periods, *J. Geophys. Res.*, *112*, A10205, doi:10.1029/2006JA012179.

Weimer, D. R. (1995), Models of high-latitude electric potentials derived with a least error fit of spherical harmonic functions, *J. Geophys. Res.*, *100*, 19,595.

Weimer, D. R. (1996), A flexible, IMF dependent model of high-latitude electric potentials having "space weather" applications, *Geophys. Res. Lett.*, *23*, 2549.

Weimer, D. R. (2001), An improved model of ionospheric electric potentials including perturbations and application to the Geospace Environment Modeling November 24, 1996, event, *J. Geophys. Res.*, *106*, 407.

Weimer, D. R. (2005), Improved ionospheric electrodynamic models and application to calculating Joule heating rates, *J. Geophys. Res.*, *110*, A05306, doi:10.1029/2004JA010884.

Wygant, J. R., R. B. Torbert, and F. S. Mozer (1983), Comparision of S3-3 polar cap potential drops with the interplanetary magnetic field and models of magnetopause reconnection, *J. Geophys. Res.*, *88*, 5727.

Zhang, S.-R., J. M. Holt, and M. McCready (2007), High latitude convection based on long-term incoherent scatter radar observations in North America, *J. Atmos. Sol.-Terr. Phys.*, *69*, 1273.

Zmuda, A. J. (1966), Ionization enhancement from Van Allen electrons in the South Atlantic Magnetic Anomaly, *J. Geophys. Res.*, *71*, 1911.

E. D. Pettigrew and S. G. Shepherd, Thayer School of Engineering, Dartmouth College, 8000 Cummings Hall, Hanover, NH 03755, USA. (pettigrew@dartmouth.edu)

J. M. Ruohoniemi, Bradley Department of Electrical and Computer Engineering, Virginia Polytechnic Institute and State University, 302 Whittemore Hall, Blacksburg, VA 24061, USA.